

Article

Stability of highly soluble ferrocyanides at neutral pH for energy-dense flow batteries

David Reber,^{1,5,7,*} Jonathan R. Thurston,² Maximilian Becker,^{3,4} and Michael P. Marshak^{1,2,6,*}

SUMMARY

Ferrocyanides and ferricyanides are among the most employed positive electrolyte materials in aqueous flow battery research, but the limited solubility of commonly available sodium and potassium salts is a critical factor limiting application at scale. Here, we systematically study the cation-dependent solubility of these materials and, importantly, the cation-dependent stability of the anion in aqueous solution. For $\text{Li}_4\text{Fe}(\text{CN})_6$, we report a maximum solubility of 2.3 M and show stable cycling of a 2 M symmetric cell, corresponding to electrolyte capacities of 54 Ah L^{-1} , over 200 days. We also demonstrate solubilities of 1.6 M for ammonium and calcium salts and investigate the pronounced anion decomposition observed in the presence of ammonium cations. Our observations lead to a discussion of challenges associated with the osmotic strength of concentrated electrolytes that employ ions with high charge states, such as ferrocyanide.

INTRODUCTION

Decarbonizing the power grid requires immense storage capacity to manage the intermittent nature of renewable energy sources, and giant batteries are becoming an integral part of modern and increasingly decentralized power grids. Because of technological maturity and decreased cost in recent years, lithium-ion batteries currently dominate this sector. However, for long-duration storage, typically more than 8 h, alternative technologies are becoming more competitive, and redox flow batteries (RFB) are being recognized as a particularly promising technology because of their unique design, which decouples energy and power elements.^{1–6} Tremendous research and commercialization efforts over the past four decades have resulted in multiple promising RFB chemistries, but large-scale deployment is still hindered by high chemical cost and raw material price fluctuations as well as the corrosive nature of electrolytes used in, e.g., all-vanadium or zinc-bromine RFBs.^{7–9} Although optimization efforts have primarily focused on these two chemistries,^{10–12} recent research has heavily focused on organic active materials. Several candidates with high solubility greater than 1 M, some with multi-electron redox properties, have successfully been demonstrated, but chemical instability and, often, a short cycle life are generally identified as major hurdles that need to be overcome.^{3,4,13–15} Another promising class of materials are metal-organic chelates, which are emerging as a high-performing family of economically viable compounds for aqueous flow batteries. Potassium chromium 1,3-propylenediaminetetraacetate (KCrPDTA), for example, a negative electrolyte (anolyte) material, enables capacities of up to 40 Ah L^{-1} and cell voltages as high as 2.1 V when coupled with a bromide-positive electrolyte (catholyte).^{16–19} The ferro-ferricyanide redox couple has remained the most used catholyte material, largely because of excellent kinetics, a redox potential well within the limitations of aqueous electrolytes, and low cost and high availability of the potassium and sodium salts.^{16–18} These anions, important

¹Renewable and Sustainable Energy Institute, University of Colorado Boulder, Boulder, CO 80303, USA

²Department of Chemistry, University of Colorado Boulder, Boulder, CO 80309, USA

³Empa, Swiss Federal Laboratories for Materials Science and Technology, 8600 Dübendorf, Switzerland

⁴ETH Zürich, Department of Materials, 8093 Zürich, Switzerland

⁵Twitter: @dreber1337

⁶Twitter: @MichaelMarshak

⁷Lead contact

*Correspondence: david.reber@colorado.edu (D.R.), michael.marshak@colorado.edu (M.P.M.) <https://doi.org/10.1016/j.xcrp.2022.101215>



precursors for pigments and catalysts, have been the subject of innumerable studies since the early 19th century, their reactivity and behavior in aqueous solution have been studied in detail,^{20–27} and almost every imaginable combination of cations with ferrocyanide anions has been described to some extent.^{28–30} However, the low solubility of the commonly available salts (0.56 M for $\text{Na}_4\text{Fe}(\text{CN})_6$ and 0.76 M for $\text{K}_4\text{Fe}(\text{CN})_6$) and the poor stability in acidic and potentially also highly basic electrolytes have been recognized as major limitations,^{31–33} and significant research efforts are geared toward developing improved catholytes.^{34–38} Capitalizing on the excellent kinetics of the ferro-ferricyanide redox couple while addressing solubility limitations, cation engineering has recently been rediscovered to synthesize more soluble ferrocyanides for flow battery applications.^{18,31,39} For example, ammonium ferrocyanide ($(\text{NH}_4)_4\text{Fe}(\text{CN})_6$), which has a solubility of up to 1.6 M, was recently coupled with an organic viologen-based anolyte, exhibiting good cycling stability at close to 1 M electrolyte concentration.³¹

Addressing the stability of ferrocyanides, the anions' photosensitivity was already studied more than a century ago,^{26,27,40,41} and instability in acidic and basic environments is heavily debated in the literature.^{24,25,27} For example, CN^-/OH^- ligand exchange when cycling ferrocyanides at high pH was identified as the main cause of capacity degradation,⁴² but this mechanism was soon after disputed, identifying water oxidation at high pH as the primary cause of capacity loss.⁴³ The light sensitivity of these anions was only recently recognized by battery researchers,^{32,33} and long-term stability of ferrocyanides in neutral pH electrolytes is still underexplored. Cycling data of batteries using ferrocyanide catholytes are often recorded over only a few days, which, as we show below, is not enough to demonstrate cation-dependent decomposition reactions at neutral pH.

Here we study the cation-dependent performance of various ferrocyanides and show that lithium and calcium ferrocyanide are promising materials with very high solubilities of up to 2.3 M (lithium) and 1.6 M (calcium) and suitable cation transport properties across commonly employed cation exchange membranes. Ammonium salts, on the other hand, show severe anion decomposition in long-term experiments. Using lithium, we demonstrate very stable cycling in symmetric flow cells with electrolyte concentrations of up to 2 M, corresponding to electrolyte capacities of 53.6 Ah L^{-1} , the highest value reported to date for hexacyanoferrate electrolytes. We report the crystal structures, some for the first time, of lithium, ammonium, and calcium ferro- and ferricyanides, clarifying hydration numbers previously unknown or contested in the literature,^{20,31} and explore the transport mechanism of ammonium cations across the membrane. Systematically surveying the cation-dependent stability of ferrocyanide electrolytes near neutral pH, we discuss decomposition pathways that need to be considered when cycling ferrocyanides for extended amounts of time at high concentrations. Finally, we point out that, for storing one electron with ferrocyanide, five ions must be solvated, and we discuss challenges, such as osmotic imbalance, that arise from the high ionic strength of concentrated electrolytes based on such high-charge-state ions. This work can thus serve as a key reference for the large community of researchers working with ferro- and ferricyanides, covering multiple aspects of the anions' chemistry with regard to battery applications.

RESULTS AND DISCUSSION

Cation-dependent solubility of ferrocyanide and ferricyanide

The room temperature solubilities of lithium, sodium, potassium, rubidium, cesium, ammonium, calcium, and magnesium ferrocyanide and ferricyanide salts are shown

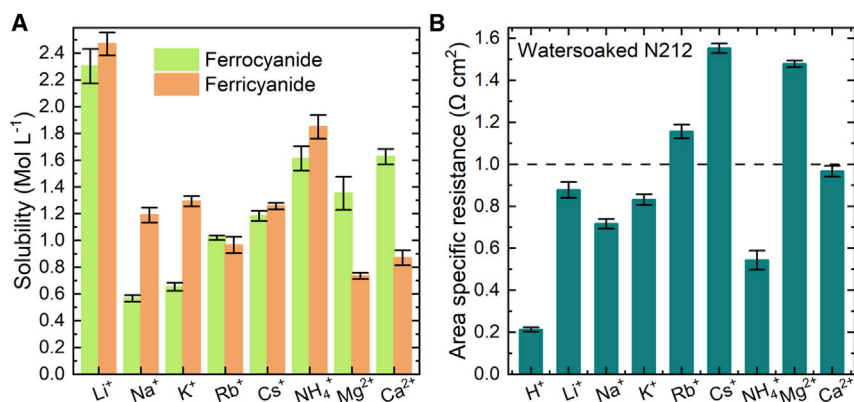


Figure 1. Highly soluble ferrocyanides

(A) Solubilities of ferrocyanide and ferricyanide salts in water at room temperature. For alkali earth ferricyanides, there are two anions per formula unit of salt.

(B) ASR in $\Omega \text{ cm}^2$ of 1 M chloride solutions in an RFB assembled with a water-soaked N212 membrane.

Error bars in (A) and (B) are standard deviations for experiments with 3 independently measured samples.

in Figure 1A and Table S1. Error bars in the figure are standard deviations for experiments with 3 independently measured samples. Ferricyanides are generally more soluble than ferrocyanides, and the solubility increases with cation size for alkali and alkali earth salts, except for lithium, which exhibits much higher solubility than the other compounds. This is in agreement with the typically high solubility of lithium salts,^{18,44} whereas sodium, potassium, ammonium, rubidium, and cesium ferrocyanides show a solubility comparable with previous reports.^{18,31} The solubility of lithium ferrocyanide reported here (2.3 M) is much higher than the value of 1.2 M reported previously by our group.¹⁸ Analysis via flame emission spectroscopy revealed that the 1.2 M soluble lithium ferrocyanide sample from our previous study contained a less soluble potassium impurity of ~1% (Figure S1), leading to an underreported maximum solubility. Flame emission spectroscopy was hence used to confirm the absence of potassium in all samples that were prepared via cation exchange from $\text{K}_4\text{Fe}(\text{CN})_6$, and purity was validated by elemental analysis. Calcium and magnesium salts are included here because their solubility was previously only described as “high” but never quantified.²⁸

Cation-dependent membrane resistance

Transport of cations across membranes is another critical parameter for flow battery applications because high membrane resistance results in poor power performance and low energy efficiency of a cell. A study on highly soluble active species based on substituted alkylammonium cations reported poor cell performance because of high resistance toward transport of such cations across the membrane.¹⁸ This demonstrates that, although cation engineering can be an excellent tool to maximize solubility, maintaining low membrane resistance remains challenging. Calculations have shown that, for aqueous flow batteries to be competitive, the area specific resistance (ASR) of the cell, which is dominated by the membrane transport properties, needs to be below $1.5 \Omega \text{ cm}^2$.^{45,46} Higher resistances would need to be compensated for by higher cell voltages, which is challenging for aqueous systems because of electrochemical stability limitations of aqueous electrolytes. For Nafion 212 (N212), a commonly employed cation exchange membrane in aqueous flow battery research, the cation-dependent membrane resistances in cells containing 1 M chloride solutions generally follow the same trend as observed for solubility (Figure 1B;

Table S2). Error bars in the figure are standard deviations for experiments with 3 independently measured samples. The alkali cations show increasing ASR with increasing cation size except for lithium, which is likely related to the large hydrated ionic radius of the latter; e.g., ~ 382 pm for Li^+ compared with 331 pm for K^+ .⁴⁷ Ammonium exhibits a lower ASR than expected from its ionic radius; NH_4^+ and Rb^+ have a crystal radius of ~ 148 pm but show an ASR of $0.54 \Omega \text{ cm}^2$ and $1.15 \Omega \text{ cm}^2$, respectively.⁴⁷ This is also seen when comparing the hydrated ionic radii, ~ 331 pm for NH_4^+ compared with ~ 329 pm for Cs^+ , but the latter shows a three times larger ASR of $1.55 \Omega \text{ cm}^2$, in excellent agreement with previous studies.^{18,48} The high mobility of ammonium across N212 membranes was previously explained by the hydrogen bonding capabilities of the cation and partial proton conduction via the Grotthuss mechanism and will be discussed below.^{18,49,50} The earth alkali metals show surprisingly low ASR values, given their large hydrated ionic radii of ~ 428 pm and 412 pm for Mg^{2+} and Ca^{2+} , respectively.⁴⁷ Based on their high solubility above 1.5 M and ASR below $1 \Omega \text{ cm}^2$, we focus on lithium, ammonium, and calcium salts for the remainder of this study.

Crystal structures

The structures and stoichiometries obtained from single-crystal XRD refinement are reported here for the first time for $\text{Li}_4\text{Fe}(\text{CN})_6 \cdot 8 \text{ H}_2\text{O}$, $\text{Ca}_2\text{Fe}(\text{CN})_6 \cdot 11 \text{ H}_2\text{O}$, $\text{Ca}_3(\text{Fe}(\text{CN})_6)_2 \cdot 2 \text{ H}_2\text{O}$, and $(\text{NH}_4)_3\text{Fe}(\text{CN})_6$, and improve previous reports for $\text{Li}_3\text{Fe}(\text{CN})_6 \cdot 7 \text{ H}_2\text{O}$ (Figure S2).²² Basic crystallographic data are summarized in Table S3. The layered structure of these compounds indicates that they may be promising candidates for electrode materials, as evidenced by previous reports suggesting high H_3O^+ and NH_4^+ conductivity in $(\text{NH}_4)_4\text{Fe}(\text{CN})_6$.⁵¹

Rate performance of symmetric cells with concentrated electrolytes

The cation-dependent cycling performance of lithium, ammonium, and calcium electrolytes at high concentrations was assessed in symmetric flow cells containing 10 mL 1.5 M ferrocyanide solutions as catholyte and 10 mL 1.5 M ferricyanide solutions as anolyte with the respective cations and no additional buffers or additives. The electrolytes were sparged with nitrogen for 2 min, sealed in test tubes with Parafilm and wrapped in aluminum foil to avoid exposure to light. Five charge/discharge cycles were performed at ± 25 , ± 50 , ± 75 , and $\pm 100 \text{ mA cm}^{-2}$ each, with cutoff voltages of 0.4 V for the charge and -0.4 V for the discharge (Figures 2A–2C). Stable cycling was observed at each current density with all three cations, whereas the average capacity utilization decreased from 99.5% at $\pm 25 \text{ mA cm}^{-2}$ to 93.4% at $\pm 100 \text{ mA cm}^{-2}$ with lithium, 99.9%–98.5% with ammonium, and 99.6%–95.2% with calcium. Coulombic efficiencies average 99.99% or greater for all three electrolytes at all current densities, with some fluctuations being explained by splashing of electrolyte up the test tubes' walls, resulting in a temporary "loss" of capacity. The rate performance agrees well with the increasing polarization shown in the voltage profiles at each current density (Figures 2D–2F) and follows the trends in membrane resistance (Figure 1B; Table S2). Lithium, however, underperforms compared with calcium, given the slightly higher membrane resistance and lower ionic conductivity with the latter cation (Figure S3A; Table S4). This is likely related to the higher viscosity of concentrated lithium- compared with calcium electrolytes because electron transfer kinetics are decreased with increasing viscosity (Figure S3B; Table S4).⁵² The excellent rate performance of the ammonium electrolyte is in agreement with low membrane resistance, low viscosity, and high conductivity and matches a previous study.³¹ The lithium and calcium electrolytes present only the second report of cycling ferro- and ferricyanide at such high concentrations.

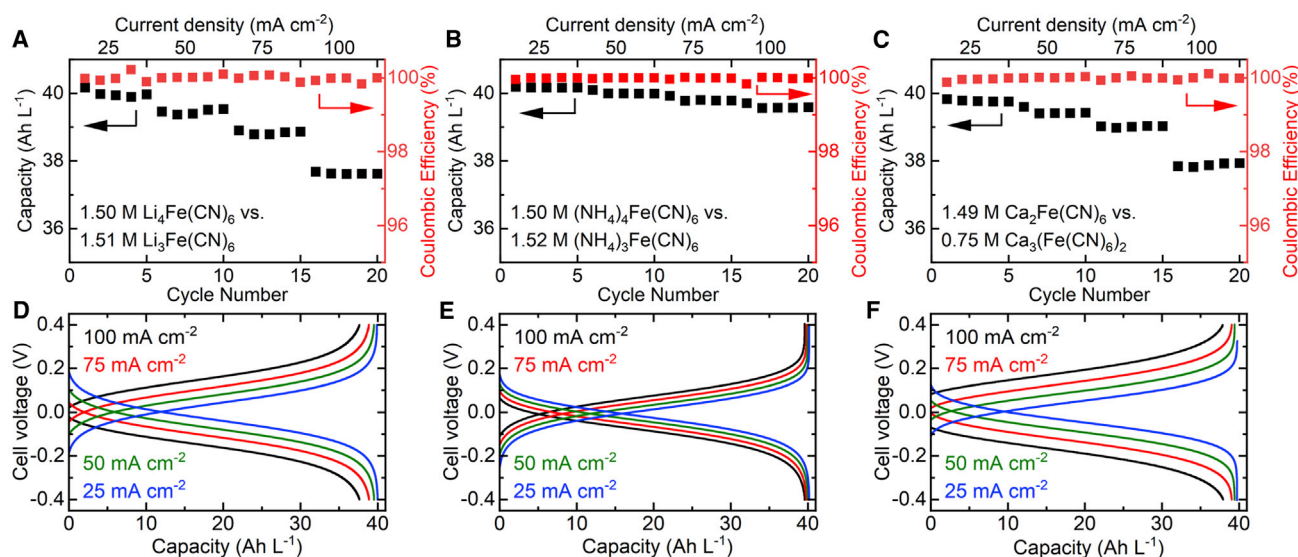


Figure 2. Rate performance of capacity-balanced 1.5 M symmetric cells

(A–C) Discharge capacity and Coulombic efficiency at ± 25 , ± 50 , ± 75 , and ± 100 mA cm⁻² for 1.5 M lithium (A), ammonium (B), and calcium (C) electrolytes.

(D–F) The corresponding voltage profiles.

Cyclic voltammetry suggests that the analyte remains intact after synthesis via cation exchange from K₄Fe(CN)₆ and is freely diffusing with all cations, yielding diffusion coefficients on the same order of magnitude, $\sim 5\text{--}10 \times 10^{-6}$ cm² s⁻¹ (Figures S4 and S5; Table S5). The values follow the ionic conductivity of the respective electrolytes when compared at the same ionic strength. As demonstrated by the pronounced differences in ionic conductivity and viscosity between lithium, ammonium, and calcium electrolytes (Table S4), ion pairing at higher concentrations is very likely to affect the diffusivity of the analyte²¹ and should be examined in future work; e.g., via pulsed-field gradient NMR experiments and molecular dynamics simulations.

Ammonium versus proton transport

As noted above, the resistance toward transport of ammonium cations across the N212 membrane is lower than expected from the ionic radius of the cation and was previously explained by extensive hydrogen bonding of the cation and contribution of Grotthuss-like proton transport (i.e., proton hopping), to the overall ionic conductivity and transport across the membrane.¹⁸ If this hypothesis were true, then the pH of the anolyte and catholyte should change significantly while cycling. During charging, for example, the ferrocyanide catholyte should increase in pH when cations (i.e., protons) travel to the ferricyanide half-cell, in turn resulting in a decrease in pH in the ferricyanide anolyte. The opposite would then occur upon discharging. Because the stability of the ferrocyanide anion is pH dependent,^{24,25,27} such a pH swing could significantly affect the cycling stability of the electrolyte. We therefore repeated the experiments shown in Figure 2 and recorded the pH of anolytes and catholytes during cycling. With all three cations, the catholyte pH decreases during charging, whereas the anolyte pH increases as cations enter the electrolyte, indicating that the cations that are transported across the membrane are not primarily protons (Figure 3). The observed trend rather corresponds to the fraction of the tetravalent Brønsted base ferrocyanide versus the trivalent base ferricyanide in each electrolyte.²⁴ A 0.5 M K₄Fe(CN)₆ solution of ferrocyanide, for example, has a

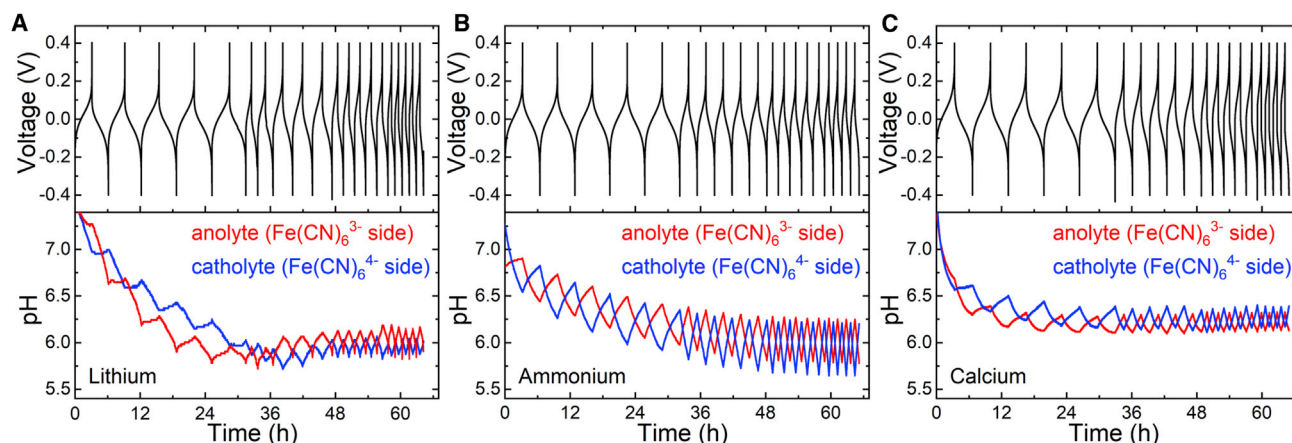


Figure 3. Evolution of pH in 1.5 M symmetric cells

(A–C) Voltage profiles at ± 25 , ± 50 , ± 75 , and $\pm 100 \text{ mA cm}^{-2}$ for 1.5 M lithium (A), ammonium (B), and calcium (C) electrolytes.

pH of ~ 9.4 , which decreases linearly with increasing fractions of ferricyanide (Figure S6). For this experiment, the potassium salt was chosen to exclude any effects on pH imposed by the preparation method (cation exchange and acid-base reaction) of the lithium and ammonium salts. The fluctuation of ~ 0.5 pH units upon cycling 1.5 M electrolytes shows that the pH difference between charged and discharged states increases with higher concentrations, in agreement with Luo et al.³¹ Fresh pH 7 calibration solutions were then measured with pH probes that had been submerged in the 1.5 M electrolytes during the cycling experiment, and values of 5.5–6 were recorded in all cases, suggesting that the overall drift of approximately one pH unit observed throughout the experiments can be assigned to drifting of the pH electrodes, likely because of changing composition of the filling solutions. For the calcium cell, the pH probe was filled with CaCl_2 because with a KCl filling, the potassium ions leaking from the pH probe caused precipitation of $\text{CaK}_2\text{Fe(CN)}_6$ on the pH probe, eventually leading to cell failure (Figure S7A). For the lithium cell, a LiCl filling solution was employed because the high concentration of lithium cations in the 1.5 M $\text{Li}_4\text{Fe(CN)}_6$ electrolyte resulted in erroneous pH measurements because of a pronounced alkali effect and large junction potentials (Figure S7B).⁵³ For the ammonium cell, a standard KCl filling was employed because no precipitation was observed, and ammonium and potassium mobilities are nearly identical, minimizing junction potentials.⁵⁴ We conclude that Grotthuss-like proton hopping across the membrane is not responsible for the excellent rate performance of ammonium electrolytes in flow batteries using N212 cation exchange membranes. Having excluded this process, it remains an open question why ammonium cations are so easily transported across the N212 membrane.

Cycling stability of symmetric cells with concentrated electrolytes

The long-term cycling stability of 1.5 M electrolytes was examined in symmetric cells by cycling at $\pm 75 \text{ mA cm}^{-2}$ for 470 cycles, corresponding to cycling times of almost 40 days. The lithium cell shows excellent stability over the long-term experiment, previously never performed over a comparable time frame (Figure 4A). Although some capacity loss can be explained by splashing in the electrolyte reservoir, the slightly increasing polarization in the voltage profiles indicates a growing cell resistance over time. This results in the cell reaching the voltage cutoffs prematurely, decreasing the time spent charging/discharging, resulting in decreasing utilized capacity (Figure 4B). Such increasing cell resistance can be explained by growing N212

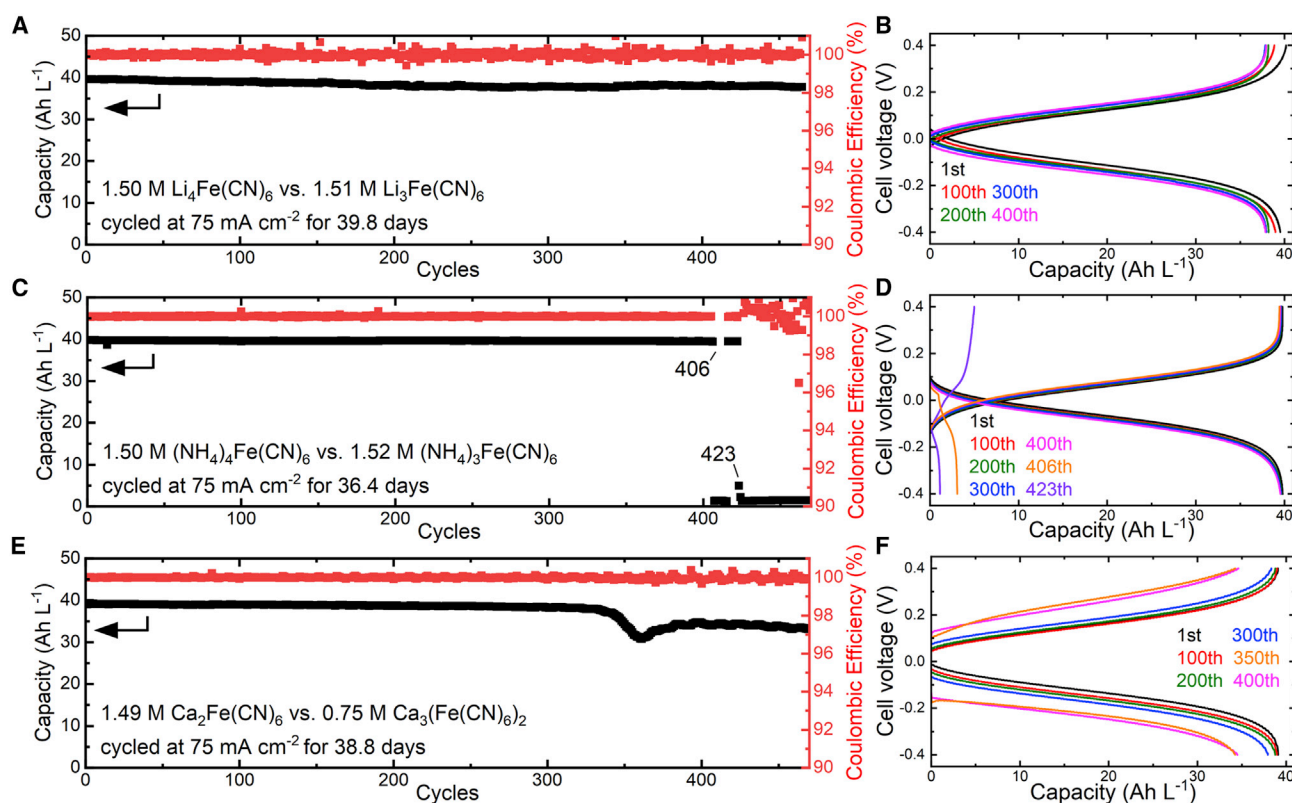


Figure 4. Long-term cycling stability of capacity-balanced 1.5 M symmetric cells

(A, C, and E) Discharge capacity and Coulombic efficiency at $\pm 75 \text{ mA cm}^{-2}$ for 1.5 M lithium (A), ammonium (C), and calcium (E) electrolytes. (B, D, and F) The corresponding voltage profiles.

membrane resistance with longer exposure to cations other than protons.¹⁸ A constant voltage step after the galvanostatic step could prevent such apparent capacity fading because of resistances not related to the active material itself.⁵⁵ In agreement with quantitative current efficiencies, no signs of decomposition were observed, and the fully discharged anolyte and catholyte were clear after the 40-day experiment (Figure S8A). Still, the apparent capacity fade rate of this cell is 0.0101% per cycle and 0.1173% per day, which can likely be attributed to the abovementioned lack of a constant voltage step and splashing.

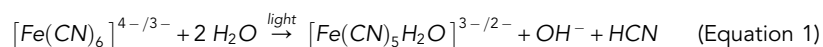
The ammonium cell showed excellent performance over almost 400 cycles, and no increase in cell resistance was observed, as indicated by the nearly perfect overlap of voltage profiles (Figures 4C and 4D). The electrolytes did, however, show increasingly green discolorations and haziness during cycling, suggesting formation of fine colloids. After 406 cycles, the cell failed during the discharge half-cycle, followed by partial recovery and eventually complete failure after 423 cycles. Flushing the cell with water after the experiment afforded a turbid green solution (Figure S8B), and upon disassembly the electrode sheets were found to be covered with a fine turquoise solid. We suspect that this precipitate continuously formed during the experiment and, over the long time frame of our experiment, accumulated in the electrode felt until, eventually, enough active electrode surface area was covered to impede cycling of the cell. The electrolytes were fully discharged in a cell with fresh electrodes and showed strong discolorations, dark brown with fine brown precipitates for the ferricyanide side and dark green and hazy for the ferrocyanide side (Figure S8C).

The calcium cell showed excellent stability for more than 300 cycles, followed by a decrease in capacity and strong increase in cell resistance at around 350 cycles. This is followed by a steady decline over the remaining ~200 h of cycling (Figures 4E and 4F). Upon full discharge, the electrolytes were clear (Figure S8D), comparable with the Li cell, but the electrodes were partially covered with a fine white precipitate (Figure S9A). This is explained by formation of calcium carbonate from absorption of atmospheric carbon dioxide because the electrolytes were not hermetically sealed from the ambient atmosphere. A second cell was assembled using airtight containers, and for this cell, outstanding stability with no comparable capacity fading was observed, supporting the above interpretation (Figure S9B).

The timescale of these experiments, much longer than previously demonstrated, clearly shows that ammonium ferro- and ferricyanide are susceptible to decomposition over prolonged periods of time, even at neutral pH. Lithium and calcium salts, on the other hand, are promising under the right conditions; i.e., using membranes optimized for Li^+ or Ca^{2+} transport and minimal exposure to ambient air in the case of calcium. Because ferrocyanide forms a turquoise precipitate in the presence of free iron(II) cations and ferricyanide a brown precipitate in presence of free iron(III) ions, our experiments indicate formation of free iron cations in ammonium electrolytes; e.g., by decomposition of the anions (Figures S10A and S10B). Prussian blue is only formed when an excess of free iron is present (Figure S10C).⁵⁶ In the following, we investigate the cation-dependent stability of ferrocyanide solutions.

Cation-dependent stability of ferrocyanide electrolytes

The effect of light and air exposure on 0.1 M ferrocyanide solutions was studied over time to assess the anions' stability in the presence of various cations. Ferrocyanide solutions were adjusted to pH 7 with dilute HCl, and the samples were sparged with nitrogen or air for 2 min and then stored under a fluorescence lamp or in the dark. The pH of the solutions was tracked over time, and the ratio of ferricyanide to ferrocyanide was determined via UV-visible (UV-vis) spectrophotometry (Figure 5 and S11). After measurements were performed, the samples were again sparged with nitrogen or air before storage. For lithium, sodium, potassium, and calcium electrolytes, the pH of the solutions quickly increases over 1–2 weeks, independent of conditions, and then asymptotes to a value between 8.5 and 10.5 over 4 months, the natural pH range of ferrocyanide solutions, as discussed above (Figure S6). Concurrently, a small amount of ferricyanide is formed over time, according to UV-vis analysis. The ratio of ferricyanide to ferrocyanide instead of absolute concentrations is displayed here to minimize the effect of dilution inaccuracy between samples. While sparging with nitrogen only shows a small effect, storage in light results in a stronger yellow discoloration, larger pH increase, and more pronounced formation of the oxidized anion, in agreement with the long-known photolysis of ferrocyanide or ferricyanide:^{26,27,40,41}



As only recently recognized by researchers in the flow battery community,^{32,33} it is critical to evaluate these materials in the dark for consistent results, and the effect of light alone is worth emphasizing here because photolysis can largely be prevented by wrapping electrolyte containers in, e.g., aluminum foil (Figure S12). The samples that were stored in the dark showed less discoloration, a smaller pH change, and only a minuscule fraction of the oxidized anion, suggesting high stability of ferrocyanide at near-neutral pH when stored in the dark, in agreement with Fell et al.³² In the air-exposed calcium samples, a minute amount of an off-white

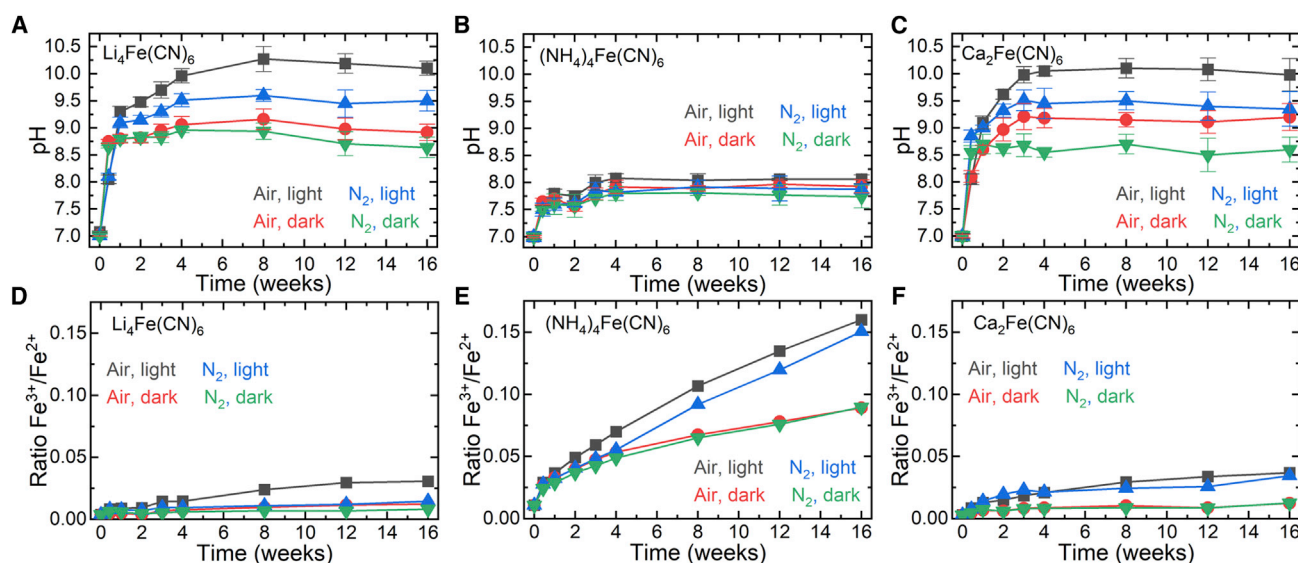


Figure 5. Cation-dependent aging of dilute ferrocyanide solutions

(A–C) Evolution of pH over time in 0.1 M lithium (A), ammonium (B), or calcium (C) electrolytes when stored in light or in the dark, and when sparged with nitrogen or air.

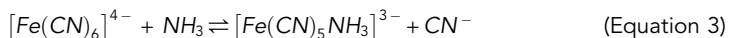
(D–F) Corresponding evolution of the ferricyanide to ferrocyanide ratio.

Error bars in (A)–(C) represent standard deviations for experiments with 3 samples, measured once with three separate pH probes each. Samples in (D–F) were measured in triplicate with resulting standard deviations of the Fe³⁺/Fe²⁺ ratio <0.001; error bars are too small to be visible and were omitted here for clarity.

precipitate was observed, which we ascribe to formation of calcium carbonate from atmospheric carbon dioxide, as discussed above (Figure 4E). This was not observed in the nitrogen-sparged calcium samples and supports the hypothesis, discussed at length previously,^{32,43} that atmospheric carbon dioxide is absorbed by the electrolytes.³² ¹³C NMR analysis of lithium, sodium, potassium, and calcium ferrocyanide solutions that were stored in the dark for 4 months do not show any resonances other than the one at 177 ppm corresponding to ferrocyanide anions, supporting our analysis (Figure S13A). Samples that were stored in light show a slightly suppressed resonance at 177 ppm because of the presence of small amounts of paramagnetic iron(III) species, in agreement with our UV-vis analysis (Figure S13B).⁵⁷

With ammonium cations, on the other hand, the pH of the sample solutions stabilizes below 8, and the solutions contain much larger fractions of the oxidized anion (Figures 5B and 5E). A fine turquoise precipitate, like the one observed in the 1.5 M symmetric cell (Figures 4C, S8B, and S8C), formed under all storage conditions, and the distinct smell of ammonia became noticeable. This suggests that ammonium cations buffer pH changes in the solution (the pK_a of NH₄⁺ is 9.25) by consuming hydroxide ions, which forms ammonia and water (Equation 2), and, when stored in light, drives the equilibrium in Equation (1) forward, accelerating decomposition of the anion. This is in excellent agreement with the stable pH in the ammonium buffer range, large fraction of iron(III) species seen in UV-vis, and, hence, completely suppressed ¹³C NMR signal (Figure S13B) observed when storing (NH₄)₄Fe(CN)₆ solutions over a prolonged period of time. This behavior was also observed with samples that were stored in the dark; large fractions of iron(III) species are measured in UV-vis (Figure 5E), and ¹³C NMR analysis showed a mostly suppressed resonance at 177 ppm (Figure S13A). This indicates that ammonium-derived ammonia accelerates anion decomposition and that ligand exchange may not only

be a photocatalytic process according to Equation (1) but can be chemically driven in the presence of ammonium cations, eventually resulting in formation of free iron cations:^{33,58}



Free iron cations are precipitated as brown solids, as observed for cycled ammonium ferricyanide electrolytes (Figure S8C), likely in the form of $\text{Fe}(\text{OH})_3$, because Prussian brown or ferric ferricyanide, $\text{Fe}^{3+}\text{Fe}^{3+}(\text{CN})_6 \cdot 2\text{H}_2\text{O}$, should only form in the presence of excess free iron(III) (Figure S10).^{33,58} Formation of a turquoise precipitate in ferrocyanide electrolytes also indicates formation of free iron according to the above pathways and precipitation of $\text{Fe}(\text{OH})_2$ or what is commonly referred to as “soluble Prussian blue,” $\text{M}^+\text{Fe}^{3+}\text{Fe}^{2+}(\text{CN})_6$ (M = cation), a turquoise colloid.^{20,56,59–61}

The ammonium samples were then electrochemically reduced to convert all paramagnetic iron(III) species back to diamagnetic low-spin ferrocyanide, so ^{13}C NMR could be employed to probe the presence of cyanide ions, which would have a resonance at 165 ppm (Figure S14A). No such resonance was observed in either electrolyte (Figure S14B). We attribute this to the very high volatility of HCN, which is formed in cyanide solutions at pH 8 (the pK_a of HCN is 9.21) or via decomposition of NH_4CN . Sparging the samples with air or nitrogen each time a sample for UV-vis analysis was collected thus likely removed cyanides from solution.

Anion decomposition is more pronounced under acidic conditions, where protonation of the anion below pH 4 significantly accelerates ligand exchange, resulting in stronger yellow discoloration and, eventually, formation of free iron ions,^{24,25} leading to formation of a turquoise precipitate in ferrocyanide electrolytes or brown precipitates in ferricyanide electrolytes (Figures S15 and S16). At pH 3, we even observed formation of Prussian blue, $\text{Fe}^{3+}_4[\text{Fe}^{2+}(\text{CN})_6]_3$, which only forms when an excess of free iron is available, indicating complete decomposition of a large fraction of the anions.^{20,56,59–61} These reactions can also take place in the solid state,^{40,58} as evidenced by solid $(\text{NH}_4)_4\text{Fe}(\text{CN})_6$ samples turning green when stored in air; Luo et al.³¹ suggest lyophilization (freeze-drying) of the material after synthesis, and solid ferrocyanides can even decompose upon grinding.⁶² We conclude that ammonium as a cation is not suitable for ferrocyanide electrolytes, even at neutral pH, whereas alkali and earth-alkali ferrocyanide electrolytes are very stable when stored in the dark and sealed from ambient air to prevent formation of carbonates. The facts that hexacyanoferrate instability at low pH has been established for decades and that its stability in basic environments is still disputed highlights the need to critically reassess the performance of these materials, the most used catholyte material in the aqueous flow battery community, over longer time frames than the handful of days typically reported.

Testing 2 M Li electrolytes

$\text{Li}_4\text{Fe}(\text{CN})_6$ is identified as a highly soluble and, more importantly, very stable catholyte material. Even at a record-high concentration of 2 M, reaching a critical solubility target for aqueous RFB electrolytes,⁴⁶ a capacity-balanced symmetric cell exhibits excellent stability over 200 days of cycling with an average Coulombic efficiency of 99.99% or greater and an unprecedented ferrocyanide catholyte capacity of 53.6 Ah L^{-1} in a near-neutral pH aqueous electrolyte (Figures 6A and 6B). The

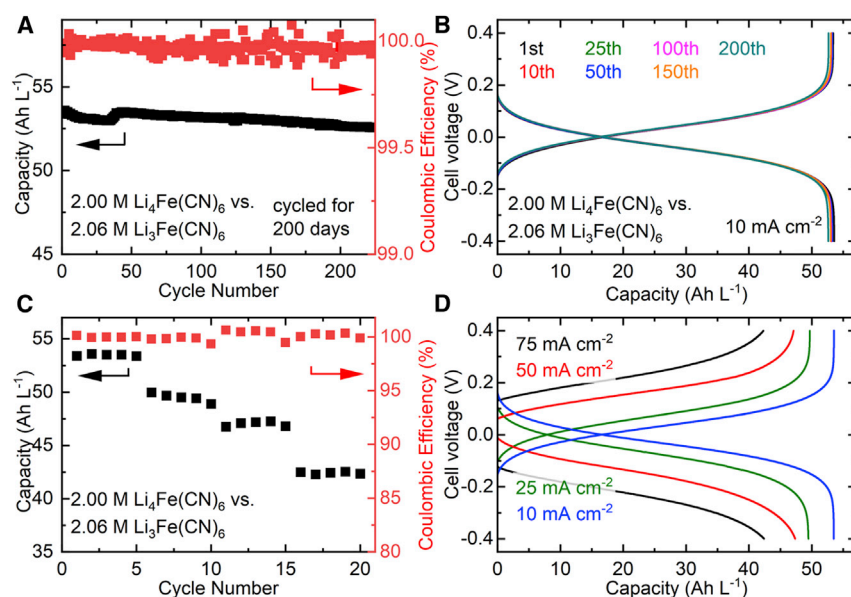


Figure 6. Capacity-balanced symmetric 2 M lithium cell

(A and B) Discharge capacity and Coulombic efficiency (A) of a cell cycled at $\pm 10 \text{ mA cm}^{-2}$ for 200 days with the corresponding voltage profiles (B). (C and D) Capacity and Coulombic efficiency (C) when cycled at ± 10 , ± 25 , ± 50 , and $\pm 75 \text{ mA cm}^{-2}$ with the corresponding voltage profiles (D).

apparent capacity fade rate of this cell is 0.0068% per cycle and 0.0077% per day. The 2 M ferrocyanide and ferricyanide electrolytes have liquidus temperatures, the point at which the mixtures convert into a fully liquid state, of -1°C and -5°C , respectively, as determined by differential scanning calorimetry (Figure S17). This agrees well with 2 M being below the maximum room temperature solubilities and clearly shows that the solutions are not supersaturated. However, high viscosity and low ionic conductivity (46.2 mPa s and 48.1 mS cm^{-1} at 25°C for 2 M $\text{Li}_4\text{Fe}(\text{CN})_6$; Figure S18; Table S4) result in decreased rate capability (Figures 6C and 6D). At $\pm 10 \text{ mA cm}^{-2}$, the 2 M cell reaches more than 99.9% capacity utilization, but increased current densities of ± 25 , ± 50 , or $\pm 75 \text{ mA cm}^{-2}$ result in lower utilization of approximately 93%, 88%, and 79%, respectively. Cycling at $\pm 25 \text{ mA cm}^{-2}$ also results in apparent capacity fading, which we explain by the liquids from the outlets of the cell not fully mixing with the bulk electrolytes in the tanks within the time frame of one cycle because of high viscosity when the tubes are not correctly arranged (Figure S19).

Balancing osmotic strength

One might argue that, for long-duration energy storage, the output power (i.e., rate capability) of the battery is of limited importance and that a 2 M $\text{Li}_4\text{Fe}(\text{CN})_6$ catholyte would be fine for slow cycling.^{6,63} However, there is another factor complicating full cell development that is seldomly discussed. Ferrocyanide is a tetravalent anion, and a 2 M $\text{Li}_4\text{Fe}(\text{CN})_6$ solution has an osmotic concentration of 10 Osm L^{-1} and ionic strength of $I = 20$, the latter being equivalent to, for example, a saturated 20 M LiCl solution. This makes it incredibly challenging to pair this catholyte with an anolyte because steep concentration gradients across the membrane result in exacerbated water transport, diluting the electrolyte of higher osmotic strength and concentrating its counterpart. For demonstrative purposes, we assembled full cells using a metal-organic chelate as anolyte material to discuss the effect of osmotic

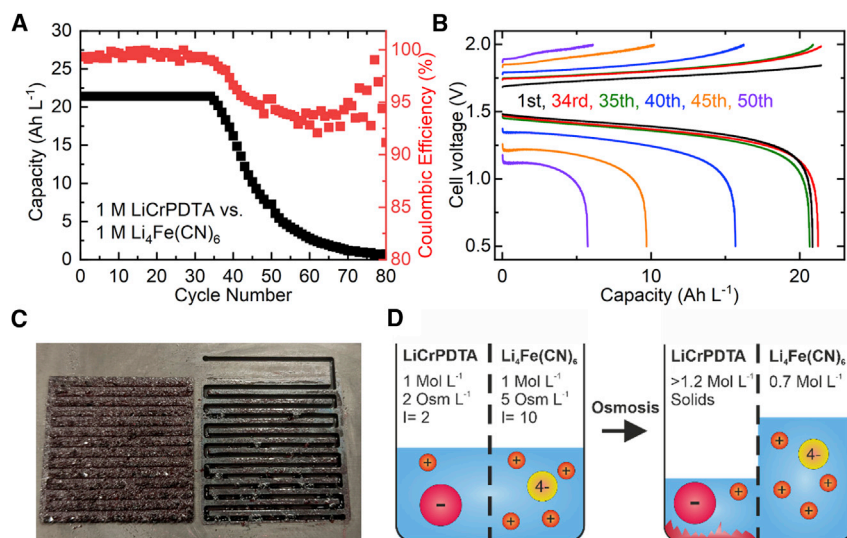


Figure 7. Full cell performance using concentrated electrolytes

(A) Discharge capacity and Coulombic efficiency at $\pm 100 \text{ mA cm}^{-2}$ for a capacity-balanced cell containing a 1 M LiCrPDTA anolyte and a 1 M Li₄Fe(CN)₆ catholyte.

(B) Corresponding voltage profiles.

(C) Clogged flow field and electrode felt recovered after the experiment.

(D) Schematic of osmotic imbalance and subsequent water transport into the electrolyte of higher ionic strength.

imbalance on cell performance. KCrPDTA exhibits a reduction potential of approximately -1.1 V versus Ag/AgCl and was previously employed in high-power flow batteries at concentrations as high as 1.5 M, and the lithium analog has a solubility of 1.2 M, making it a prime candidate for pairing with a Li₄Fe(CN)₆ catholyte.^{16–18}

In a capacity-balanced full cell using 10 mL 1 M LiCrPDTA buffered by a 0.1 M borate buffer at pH 8.4 as anolyte and 10 mL of a solution of 1 M Li₄Fe(CN)₆ + 0.1 M Li₃Fe(CN)₆ as catholyte at pH 8, we observe excellent cycling stability at 100 mA cm⁻² over 35 cycles with an average discharge voltage of 1.45 V when cycled to 80% state of charge (SoC). The upper and lower voltage limits were set at 0.5 and 2.1 V, respectively. The cell reaches a capacity of 21.4 Ah L⁻¹ at 80% SoC and an average Coulombic efficiency over those 35 cycles of more than 99.5% (Figures 7A and 7B). This corresponds to an excellent energy density per total volume of electrolytes of 15.5 Wh L⁻¹. After 29 h of cycling, however, the battery rapidly lost capacity, and the anolyte stopped flowing. Upon disassembly of the cell, we found that the anolyte side was clogged by crystalline LiCrPDTA, preventing cycling of the battery (Figure 7C), and 15 mL of catholyte with a combined ferro- and ferricyanide concentration of only 0.65 M was recovered. An unbuffered 1 M LiCrPDTA anolyte has an osmotic concentration of 2 Osm L⁻¹ and ionic strength of $I = 2$, whereas a 1 M Li₄Fe(CN)₆ catholyte has 5 Osm L⁻¹ and $I = 10$. It is therefore no surprise that water is pushed from the anolyte into the catholyte, following the osmotic gradient (Figure 7D), in this case enough to saturate the anolyte, precipitating LiCrPDTA. We also assembled full cells containing a 1.2 M anolyte and a 1.2 M catholyte or a 1 M anolyte and a 2 M catholyte, respectively, with the same outcome of rapid cell failure because of formation of solids in the anolyte half-cell (Figure S20). This demonstrates that, although this cell chemistry has a theoretical energy density per total volume of electrolytes of up to 30 Wh L⁻¹ (assuming 2.3 M Li₄Fe(CN)₆ catholyte, 1.2 M LiCrPDTA anolyte, average discharge voltage of 1.45 V, and 100% SoC),

the osmotic imbalance when using a concentrated ferrocyanide catholyte prevents reaching such high values. This highlights that, although high electrolyte capacities can be achieved with ferrocyanides, the high ionic strength of such solutions can be prohibitive for practical use.

Challenges of concentrated electrolytes

Our data show that we must include charge states of ions as a critical parameter in our efforts to develop better active materials for flow batteries. Using ferrocyanides, for example, five ions must be solvated to store just one electron. This inefficient atom economy directly affects the power performance of the battery via high viscosity and may exacerbate water transport across the membrane via high ionic strength of the electrolytes. Accordingly, our work suggests that ferrocyanides are unsuitable for flow battery systems where high energy density is a critical parameter; lithium and calcium electrolytes above 1.5 M are highly viscous, leading to decreased power performance, ammonium electrolytes are unstable over long time periods, and other sensible cations lead to insufficient solubility or excessive membrane resistance.¹⁸ The dielectric decrement (i.e., the decreased dielectric permittivity, of concentrated electrolytes) may also negatively affect mass transport in the cell stack.^{64,65}

Because energy density is of limited importance for most use cases of flow batteries,^{45,66} research should capitalize on the excellent properties of the ferro-ferricyanide redox couple rather than fixating on its limited solubility. Generally, the importance of energy density for RFBs needs to be better understood, and cost, efficiency, lifetime, and availability of materials need to be emphasized for a swift transition from lab to practical applications.

We describe highly soluble ferrocyanides and ferricyanides, focusing on lithium, ammonium, and calcium salts, and discuss their suitability for flow battery applications. We infer that the excellent rate capability of ammonium electrolytes cannot be explained by Grotthuss-like proton transport. Cycling of symmetric cells using 1.5 M electrolytes for up to 40 days and aging experiments over 4 months show that the ammonium salts are susceptible to decomposition, even at neutral pH, whereas carbonates precipitate in calcium electrolytes when exposed to ambient air. With a solubility of 2.3 M and excellent long-term stability, $\text{Li}_4\text{Fe}(\text{CN})_6$ stands out among the ferrocyanides. Excellent cycling stability over 200 days is observed for a 2 M symmetric cell, corresponding to an electrolyte capacity of 54 Ah L^{-1} , the highest value reported to date for any hexacyanoferrate-based electrolyte. However, at such high concentrations, the high charge state of ferrocyanide results in electrolytes with very high ionic strength, and pairing with an anolyte of lower osmotic strength leads to significant water transport across the membrane, which can even result in precipitation of the counter electrolyte. The charge state of ions must thus be considered when developing new active materials, and the role of energy density for RFBs needs to be better understood.

EXPERIMENTAL PROCEDURES

Resource availability

Lead contact

Further information and requests for resources and reagents should be directed to and will be fulfilled by the lead contact, D.R. (david.reber@colorado.edu).

Materials availability

This study did not generate new unique materials.

Data and code availability

All data generated or analyzed during this study are included in this article and its supplemental information files. CCDC 2213587–2213591 contain the supplemental crystallography data (crystal data: $\text{Li}_4\text{Fe}(\text{CN})_6 \cdot 8 \text{H}_2\text{O}$, deposition number 2213589; $\text{Li}_3\text{Fe}(\text{CN})_6 \cdot 7 \text{H}_2\text{O}$, deposition number 2213590; $(\text{NH}_4)_3\text{Fe}(\text{CN})_6$, deposition number 2213591; $\text{Ca}_2\text{Fe}(\text{CN})_6 \cdot 11 \text{H}_2\text{O}$, deposition number 2213588; $\text{Ca}_3(\text{Fe}(\text{CN})_6)_2 \cdot 2 \text{H}_2\text{O}$, deposition number 2213587) for this study. The data can be obtained free of charge via www.ccdc.cam.ac.uk/data_request/cif. All CIF files are included in [Data S1](#). Any additional raw data files are available from the lead author upon reasonable request.

Electrolyte materials preparation

All materials were used as received without further purification. $\text{K}_4\text{Fe}(\text{CN})_6 \cdot 3 \text{H}_2\text{O}$ (>99%) and $\text{Na}_4\text{Fe}(\text{CN})_6 \cdot 10 \text{H}_2\text{O}$ (ACS grade) were purchased from Fluka and Acros Organics, respectively, and $\text{K}_3\text{Fe}(\text{CN})_6$ (ACS grade) was purchased from LabChem. 1,3-Propylenediaminetetraacetic acid (H_4PDTA ; 99%) was purchased from Sigma-Aldrich. $\text{CrCl}_3 \cdot 6 \text{H}_2\text{O}$ (98%) was purchased from Alfa Aesar. Alkali and alkali earth hydroxides and chlorides were purchased from Fisher Chemical. Boric acid (99.5%) was purchased from Acros Organics.

Amberlyst 15H ion exchange resin was used to prepare alkali salts of the described compounds. A column of length of 20 cm and diameter of 1.5 cm were used. 20 g of resin, corresponding to a cation-capacity of 0.094 mol, were soaked in water for 5 min, loaded into the column, and flushed with 50 mL of water five times. A concentrated solution of $\text{K}_4\text{Fe}(\text{CN})_6$ or $\text{K}_3\text{Fe}(\text{CN})_6$ was then passed through the column, followed by water to elute $\text{H}_4\text{Fe}(\text{CN})_6$ or $\text{H}_3\text{Fe}(\text{CN})_6$. The product was directly eluted into a hydroxide solution containing the desired cation, and the solution was adjusted to pH 8 before drying on a watch glass. An amount of starting material corresponding to 70% of the resin's cation capacity was used. Drying at pH < 5 resulted in green decomposition products, and drying at pH > 10 led to formation of white carbonate impurities. Amorphous materials can be obtained by precipitation of the product with ethanol. Preparation via the hydrogen form of the salt was chosen for increased yield (quantitative) and purity compared with functionalization of the resin with the target cation; see Thurston et al.⁶⁷ for a detailed discussion of resin functionalization efficiency. Successful exchange of cations was determined via flame emission spectroscopy using an in-house-built setup to track alkali cation ratios in liquid samples. The setup is described in detail in Thurston et al.⁶⁷ Briefly, 50 μL of sample solution was ionized with a torch, and the flame was monitored with a fiber-coupled optical spectrometer (Avantes AvaSpec-ULS2048L with a spectral resolution of 1.4 nm, wavelength range of 200–1,100 nm, and ILX511 2048-pixel detector). The ratio of alkali emission peaks was then used to assess the cation exchange efficiency, and samples with no potassium signal were judged to be pure.

Ca ferrocyanide was synthesized by dissolving $\text{Na}_4\text{Fe}(\text{CN})_6 \cdot 10 \text{H}_2\text{O}$ (24.2 g, 0.05 mol) in 100 mL water, followed by addition of a mixture of CaCl_2 (7.35 g, 0.05 mol) and NH_4Cl (5.35 g, 0.1 mol) dissolved in 10 mL water. The resulting $\text{Ca}(\text{NH}_4)_2\text{Fe}(\text{CN})_6$ precipitate was filtered off, washed with cold water, combined with excess $\text{Ca}(\text{OH})_2$, and heated at 80°C overnight, releasing ammonia and water. The resulting slurry was filtered, and the liquid was dried by evaporation, resulting in formation of large, needle-shaped, pale yellow $\text{Ca}_2\text{Fe}(\text{CN})_6 \cdot 11 \text{H}_2\text{O}$ crystals (16.5 g, 0.034 mol, molecular weight [MW] = 490.3 g mol^{−1}, 67.3% yield).⁶⁸ The magnesium

salt was prepared analogously. Ca and magnesium ferricyanides were prepared via bulk electrolysis of corresponding ferrocyanides versus $\text{K}_3\text{Fe}(\text{CN})_6$.

Elemental analysis of Li, ammonium, and Ca ferrocyanides was performed by Midwest Microlab: $\text{Li}_4\text{Fe}(\text{CN})_6 \cdot 8 \text{H}_2\text{O}$, calculated: C 18.77, N 21.89, H 4.2. Found: C 18.6, 22.01, 4.37. $(\text{NH}_4)_4\text{Fe}(\text{CN})_6 \cdot 1.5 \text{H}_2\text{O}$, Calculated: C 23.16, N 45.02, H 6.16. Found: C 23.47, 46.23, 5.92. $\text{Ca}_2\text{Fe}(\text{CN})_6 \cdot 11 \text{H}_2\text{O}$, Calculated: C 14.7, N 17.14, H 4.52. Found: C 17.36, N 18.28, H 3.87. The slight discrepancy for calcium ferrocyanide suggests a water content of 8–9 water molecules per formula unit, in agreement with a corresponding mass loss observed when samples are left to dry in ambient atmosphere.

LiCrPDTA was synthesized following an adapted procedure from our previously reported method.¹⁷ H_4PDTA (30.63 g, 0.1 mol) and an equivalent of $\text{LiOH} \cdot 6 \text{H}_2\text{O}$ (4.2 g, 0.1 mol) were dissolved in 80 mL water and stirred for 10 min. $\text{CrCl}_3 \cdot 6 \text{H}_2\text{O}$ (26.65 g, 0.1 mol) was then added, and the solution was refluxed overnight. The solution was cooled to 80°C and 3 equiv of $\text{LiOH} \cdot 6 \text{H}_2\text{O}$ (12.6 g, 0.3 mol) dissolved in 100 mL water were then added over 2 days with an addition funnel. The pH was adjusted to a value of 4.75, and the solution was then cooled to room temperature and concentrated by evaporation. The mixture was washed with methanol three times to remove LiCl, followed by recrystallization from aqueous solution, yielding 36.2 g crimson red $\text{LiCrPDTA} \cdot 3 \text{H}_2\text{O}$ crystals (0.087 mol, MW = 415.3 g mol⁻¹, 87.2% yield). The material was confirmed via UV-vis peaks at 506 and 382 nm.^{17,18}

Electrolyte characterization

UV-vis spectrophotometry was performed on an Agilent Cary 60 spectrophotometer with a 1.5-nm fixed spectral bandwidth. Before determining the concentration of saturated solutions, all samples were filtered through a glass frit with a pore size of 10–16 μm (Chemglass Life Sciences medium). For rubidium ferricyanide, three independent batches of material were measured three times each to verify the lower-than-expected solubility. For ferrocyanide, the absorption at 320 nm ($\epsilon = 315.6$) and for ferricyanide at 420 nm ($\epsilon = 1,130$) were considered. LiCrPDTA samples were diluted 250 \times , ferrocyanide solutions 500 \times –1,000 \times , and ferricyanide solutions 1,000–2,000 \times for measurement. Room temperature was $\sim 22^\circ\text{C}$.

Ionic conductivity was determined via impedance spectroscopy on a Bio-Logic MCS 10 in sealed 2-electrode cells equipped with Pt electrodes (Bio-Logic HTCC). The samples, 600 μL , were equilibrated for 15 min at each temperature.

Viscosity was determined with a Kyoto Electronics Manufacturing EMS-1000 electromagnetically spinning viscometer using 2-mm Al spheres. Sample volumes of 400 μL were used. The samples were equilibrated for 15 min at each temperature. Ferricyanides could not be measured because of pronounced reactivity between the electrolytes and the Al spheres.

NMR spectra were recorded on a Bruker Avance-III 400 NMR spectrometer, using a mixture of 90% sample solution and 10% D_2O .

Differential scanning calorimetry was carried out with a Netzsch STA 449 F3 simultaneous thermal analyzer. Approximately 30 mg of electrolyte sample was mixed with 1–2 mg of meso-carbon microbeads acting as a crystallization agent and sealed in Al

pans. Measurements were carried out at a scan rate of $1^{\circ}\text{C min}^{-1}$. Liquidus transitions were defined by their peak maxima.

X-ray crystallography

Single-crystal X-ray crystallography data were recorded using a Bruker D8 Quest Eco three-circle goniometer platform equipped with a Bruker APEX-II charge-coupled device (CCD) detector. A graphite monochromator was employed for wavelength selection of the Mo K α radiation ($\lambda = 0.71073 \text{ \AA}$). Data were processed using APEX III, and crystal structures were solved with the olex2.solve structure solution program in Olex2.^{69,70} Structures were visualized using VESTA.⁷¹ Single crystals of pure Li, ammonium, and Ca ferrocyanides and ferricyanides were obtained through slow water evaporation from pure solutions of the respective salts. $\text{Li}_4\text{Fe}(\text{CN})_6$ and $\text{Ca}_2\text{Fe}(\text{CN})_6$, respectively, formed pale-yellow fine (millimeters) or large (centimeters) needle-shaped crystals, whereas $(\text{NH}_4)_4\text{Fe}(\text{CN})_6$ formed almost colorless brittle platelets. $\text{Li}_3\text{Fe}(\text{CN})_6$ and $\text{Ca}_3(\text{Fe}(\text{CN})_6)_2$ formed fine red needles, and $(\text{NH}_4)_3\text{Fe}(\text{CN})_6$ formed brownish-red rhombohedral platelets. Because $(\text{NH}_4)_4\text{Fe}(\text{CN})_6$ solids turned turquoise within a few hours of exposure to ambient air, samples for crystallography had to be extracted from saturated solutions and measured immediately. No data of sufficient quality could be recorded.

Electrochemical characterization

Cyclic voltammetry was performed on a Gamry 1000 potentiostat using 1-mm-diameter glassy carbon working electrodes, Ag/AgCl reference electrodes, and Pt-wire counter electrodes (eDAQ). Beaker-type electrochemical cells with 0.6 mL of electrolyte were used. All solutions were purged with Argon for 5 min before data were collected and kept under an Argon blanket during experiments.

All battery cycling data were collected on an Arbin LBT21084HC workstation, and the flow cell setup used was described previously in detail.¹⁸ Briefly, N212 membranes (50 μm thick, $3 \times 3 \text{ cm}$) were pretreated by soaking in pure deionized water for 48 h. Two stacked sheets of GDL 39 AA carbon paper (SGL, 280 μm thick, 5 cm^2 each) were dried at 150°C in air for 24 h for improved wettability and used on each side of the membrane with a 1/64-in Viton gasket providing $\sim 25\%$ electrode compression. The cells were bolted together and tightened with a torque wrench set to 6 N m. The flow rate was controlled at 60 mL min^{-1} , and cells were cycled at room temperature, $\sim 22^{\circ}\text{C}$. Before redox-active electrolytes were used, 1 M chloride solutions were pumped through the cell for 5 min to replace protons in the membrane with target cations to prevent strong pH changes when first charging the cells.

Impedance spectroscopy was performed using a Gamry 1000 potentiostat to determine the cation-dependent ASR of flow cells containing water-soaked N212 membranes and 1 M chloride solutions with corresponding cations on both sides of the membrane. Data were collected between 500 kHz and 1,000 Hz with an amplitude of 10 mV at 10 ppd. After the measurement, the chloride solution was circulated through the cell for 1 min, and the measurement was repeated. The resistance representing the ohmic resistance of the cell was extracted from Nyquist plots by fitting the data to a model circuit and was multiplied by the electrode area (5 cm^2), giving ASR in $\Omega \text{ cm}^2$ (Figure S21).

pH tracking during cycling was performed using a Hanna HI22091-01 pH meter with analog output and Hanna HI1332B pH probe. Chronopotentiometry with no applied current was used to determine the pH meter output voltage in pH 7 and pH 10 buffer

solutions (Fisher Scientific SB107 and SB115), and the voltages were fit to a linear regression. This regression was applied to measured voltages during cycling to convert voltages to a pH value. Aging experiments were performed by measuring each sample once per time point with three separate freshly calibrated pH probes to account for any fluctuations between probes.

SUPPLEMENTAL INFORMATION

Supplemental information can be found online at <https://doi.org/10.1016/j.xcrp.2022.101215>.

ACKNOWLEDGMENTS

The information, data, or work presented herein was funded by the DOE Office of Electricity Energy Storage Program at Pacific Northwest National Laboratory through subcontract 608616. J.R.T. was supported in part by the Edward L. King Fellowship. The views and opinions of authors expressed herein do not necessarily state or reflect those of the United States government or any agency thereof.

AUTHOR CONTRIBUTIONS

D.R., conceptualization, methodology, synthesis, investigation, data curation, visualization, writing – original draft, writing – review & editing, and supervision; J.R.T., data curation; M.B., investigation; M.P.M., resources, funding acquisition, and writing – review & editing.

DECLARATION OF INTERESTS

The authors declare no competing interests.

Received: November 1, 2022

Revised: November 11, 2022

Accepted: December 8, 2022

Published: January 6, 2023

REFERENCES

- Yang, Z., Zhang, J., Kintner-Meyer, M.C.W., Lu, X., Choi, D., Lemmon, J.P., and Liu, J. (2011). Electrochemical energy storage for green grid. *Chem. Rev.* 111, 3577–3613. <https://doi.org/10.1021/cr100290v>.
- Soloveichik, G.L. (2015). Flow batteries: current status and trends. *Chem. Rev.* 115, 11533–11558. <https://doi.org/10.1021/cr500720t>.
- Li, Z., and Lu, Y.C. (2020). Material design of aqueous redox flow batteries: fundamental challenges and mitigation strategies. *Adv. Mater.* 32, 2002132. <https://doi.org/10.1002/adma.202002132>.
- Sánchez-Díez, E., Ventosa, E., Guarnieri, M., Trovò, A., Flox, C., Marcilla, R., Soavi, F., Mazur, P., Aranzabe, E., and Ferret, R. (2021). Redox flow batteries: status and perspective towards sustainable stationary energy storage. *J. Power Sources* 481, 228804. <https://doi.org/10.1016/j.jpowsour.2020.228804>.
- Perry, M.L., Rodby, K.E., and Brushett, F.R. (2022). Untapped potential: the need and opportunity for high-voltage aqueous redox flow batteries. *ACS Energy Lett.* 7, 659–667. <https://doi.org/10.1021/acsenenergylett.1c02225>.
- Albertus, P., Manser, J.S., and Litzelman, S. (2020). Long-duration electricity storage applications, economics, and technologies. *Joule* 4, 21–32. <https://doi.org/10.1016/j.joule.2019.11.009>.
- Hu, B., Luo, J., DeBruler, C., Hu, M., Wu, W., and Liu, T.L. (2019). Redox-active inorganic materials for redox flow batteries. *Encycl. Inorg. Bioinorg. Chem.* 3, 211–235.
- Skyllas-Kazacos, M., Cao, L., Kazacos, M., Kausar, N., and Mousa, A. (2016). Vanadium electrolyte studies for the vanadium redox battery—a review. *ChemSusChem* 9, 1521–1543. <https://doi.org/10.1002/cssc.201600102>.
- Wang, W., Luo, Q., Li, B., Wei, X., Li, L., and Yang, Z. (2013). Recent progress in redox flow battery research and development. *Adv. Funct. Mater.* 23, 970–986. <https://doi.org/10.1002/adfm.201200694>.
- Liu, Q.H., Grim, G.M., Papandrew, A.B., Turhan, A., Zawodzinski, T.A., and Mench, M.M. (2012). High performance vanadium redox flow batteries with optimized electrode configuration and membrane selection. *J. Electrochem. Soc.* 159, A1246–A1252. <https://doi.org/10.1149/2.051208jes>.
- Perry, M.L., Darling, R.M., and Zaffou, R. (2013). High power density redox flow battery cells. *ECS Trans.* 53, 7–16. <https://doi.org/10.1149/05307.0007/ecst>.
- Jiang, H.R., Sun, J., Wei, L., Wu, M.C., Shyy, W., and Zhao, T.S. (2020). A high power density and long cycle life vanadium redox flow battery. *Energy Storage Mater.* 24, 529–540. <https://doi.org/10.1016/j.ensm.2019.07.005>.
- Brushett, F.R., Aziz, M.J., and Rodby, K.E. (2020). On lifetime and cost of redox-active organics for aqueous flow batteries. *ACS Energy Lett.* 5, 879–884. <https://doi.org/10.1021/acsenenergylett.0c00140>.
- Lin, K., Chen, Q., Gerhardt, M.R., Tong, L., Kim, S.B., Eisenach, L., Valle, A.W., Hardee, D., Gordon, R.G., Aziz, M.J., and Marshak, M.P. (2015). Alkaline quinone flow battery. *Science* 349, 1529–1532. <https://doi.org/10.1126/science.aab3033>.
- Park, M., Ryu, J., Wang, W., and Cho, J. (2016). Material design and engineering of next-generation flow-battery technologies. *Nat. Rev. Mater.* 2, 16080–16118. <https://doi.org/10.1038/natrevmats.2016.80>.

16. Robb, B.H., Farrell, J.M., and Marshak, M.P. (2019). Chelated chromium electrolyte enabling high-voltage aqueous flow batteries. *Joule* 3, 2503–2512. <https://doi.org/10.1016/j.joule.2019.07.002>.
17. Reber, D., Thurston, J.R., Becker, M., Pach, G.F., Wagoner, M.E., Robb, B.H., Waters, S.E., and Marshak, M.P. (2022). Mediating anion-cation interactions to improve aqueous flow battery electrolytes. *Appl. Mater. Today* 28, 101512. <https://doi.org/10.1016/j.apmt.2022.101512>.
18. Waters, S.E., Thurston, J.R., Armstrong, R.W., Robb, B.H., Marshak, M.P., and Reber, D. (2022). Holistic design principles for flow batteries: cation dependent membrane resistance and active species solubility. *J. Power Sources* 520, 230877. <https://doi.org/10.1016/j.jpowsour.2021.230877>.
19. Thurston, J.R., Waters, S.E., Robb, B.H., and Marshak, M.P. (2022). Organic and metal-organic RFBs. In *Encyclopedia of Energy Storage* (Elsevier), pp. 423–435. <https://doi.org/10.1016/B978-0-12-819723-3.00082-2>.
20. Davidson, D., and Welo, L.A. (2002). The nature of prussian blue. *J. Phys. Chem.* 32, 1191–1196. <https://doi.org/10.1021/j150290a007>.
21. Eaton, W.A., George, P., and Hanania, G.I. (1967). Thermodynamic aspects of the potassium hexacyano-ferrate (III)-(II) system. I. Ion association. *J. Phys. Chem.* 71, 2016–2021. <https://doi.org/10.1021/j100866a007>.
22. Zhilov, V.I., Ilyukhin, A.B., Kotov, V.Y., Kuz'minova, Z.V., and Tsirlina, G.A. (2002). Ion association in aqueous solutions of hexacyanoferrates. *Zhurnal Neorg Khimii* 47, 1728–1731.
23. Yu, P., Yang, F., Zhao, J., and Wang, J. (2014). Hydration dynamics of cyanoferrate anions examined by ultrafast infrared spectroscopy. *J. Phys. Chem. B* 118, 3104–3114. <https://doi.org/10.1021/jp410614f>.
24. Domingo, P.L., Garcia, B., and Leal, J.M. (1987). Acid-base behaviour of the ferrocyanide ion in perchloric acid media potentiometric and spectrophotometric study. *Can. J. Chem.* 65, 583–589. <https://doi.org/10.1139/v87-102>.
25. Domingo, P.L., Garcia, B., and Leal, J.M. (1990). Acid-base behaviour of the ferricyanide ion in perchloric acid media. Spectrophotometric and kinetic study. *Can. J. Chem.* 68, 228–235. <https://doi.org/10.1139/v90-030>.
26. Foster, G.W.A. (1906). XCV.—the action of light on potassium ferrocyanide. *J. Chem. Soc. Trans.* 89, 912–920. <https://doi.org/10.1039/CT9068900912>.
27. Kolthoff, I.M., and Pearson, E.A. (1931). Stability of potassium ferrocyanide solutions. *Ind. Eng. Chem. Anal. Ed.* 3, 381–382. <https://doi.org/10.1021/ac50076a022>.
28. Comey, A.M. (1896). *A Dictionary of Chemical Solubilities* (Macmillan and Company).
29. Farrow, M. (1926). XI.—the solubilities of sodium, potassium, and calcium ferrocyanides. Part I. *J. Chem. Soc.* 129, 49–55.
30. Williams, H.E. (1915). *The Chemistry of Cyanogen Compounds and their Manufacture and Estimation* (J. & A. Churchill).
31. Luo, J., Hu, B., Debruler, C., Bi, Y., Zhao, Y., Yuan, B., Hu, M., Wu, W., and Liu, T.L. (2019). Unprecedented capacity and stability of ammonium ferrocyanide catholyte in pH neutral aqueous redox flow batteries. *Joule* 3, 149–163. <https://doi.org/10.1016/j.joule.2018.10.010>.
32. Fell, E., De Porcellinis, D., Jing, Y., Gutierrez-Venegas, V., Gordon, R., Granados-Focil, S., and Aziz, M. (2022). Long-term stability of ferri-/ferrocyanide as an electroactive component for redox flow battery applications: on the origin of apparent capacity fade. Preprint at ChemRxiv. <https://doi.org/10.26434/chemrxiv-2022-zl7l6>.
33. Hu, M., Wang, A., and Liu, T. (2022). Cycling performance and mechanistic insights of ferricyanide electrolytes in alkaline redox flow batteries. Preprint at ChemRxiv. <https://doi.org/10.26434/chemrxiv-2022-lqms7>.
34. Li, X., Gao, P., Lai, Y.-Y., Bazak, J.D., Hollas, A., Lin, H.-Y., Murugesan, V., Zhang, S., Cheng, C.-F., Tung, W.-Y., et al. (2021). Symmetry-breaking design of an organic iron complex catholyte for a long cyclability aqueous organic redox flow battery. *Nat. Energy* 6, 873–881. <https://doi.org/10.1038/s41560-021-00879-6>.
35. Hu, B., DeBruler, C., Rhodes, Z., and Liu, T.L. (2017). Long-cycling aqueous organic redox flow battery (AORFB) toward sustainable and safe energy storage. *J. Am. Chem. Soc.* 139, 1207–1214. <https://doi.org/10.1021/jacs.6b10984>.
36. Janoschka, T., Martin, N., Hager, M.D., and Schubert, U.S. (2016). An aqueous redox-flow battery with high capacity and power: the TEMPTMA/MV system. *Angew. Chem. Int. Ed. Engl.* 55, 14427–14430. <https://doi.org/10.1002/anie.201606472>.
37. Beh, E.S., De Porcellinis, D., Gracia, R.L., Xia, K.T., Gordon, R.G., and Aziz, M.J. (2017). A neutral pH aqueous organic-organometallic redox flow battery with extremely high capacity retention. *ACS Energy Lett.* 2, 639–644. <https://doi.org/10.1021/acscenergylett.7b00019>.
38. Hooper-Burkhardt, L., Krishnamoorthy, S., Yang, B., Murali, A., Nirmalchandar, A., Prakash, G.K.S., and Narayanan, S.R. (2017). A new Michael-reaction-resistant benzoquinone for aqueous organic redox flow batteries. *J. Electrochem. Soc.* 164, A600–A607. <https://doi.org/10.1149/2.0351704jes>.
39. Li, X., Yao, Y., Jia, X., Liu, C., Jian, J., Guo, B., Cui, K., Lu, S., Li, Y., and Qin, W. (2022). Lithium Ferrocyanide Catholyte for High-Capacity Aqueous Redox Flow Batteries.
40. Lofthfield, R.B., and Swift, E., Jr. (1938). The stability of dry potassium ferrocyanide. *J. Am. Chem. Soc.* 60, 3083–3084. <https://doi.org/10.1021/ja01279a504>.
41. Shirom, M., and Stein, G. (1971). Excited state chemistry of the ferrocyanide ion in aqueous solution. II. Photoaquation. *J. Chem. Phys.* 55, 3379–3382. <https://doi.org/10.1063/1.1676588>.
42. Luo, J., Sam, A., Hu, B., DeBruler, C., Wei, X., Wang, W., and Liu, T.L. (2017). Unraveling pH dependent cycling stability of ferricyanide/ferrocyanide in redox flow batteries. *Nano Energy* 42, 215–221. <https://doi.org/10.1016/j.nanoen.2017.10.057>.
43. Páez, T., Martínez-Cuevas, A., Palma, J., and Ventosa, E. (2020). Revisiting the cycling stability of ferrocyanide in alkaline media for redox flow batteries. *J. Power Sources* 471, 228453. <https://doi.org/10.1016/j.jpowsour.2020.228453>.
44. Reber, D., Kühnel, R.S., and Battaglia, C. (2017). High-voltage aqueous supercapacitors based on NaTFSI. *Sustain. Energy Fuels* 1, 2155–2161. <https://doi.org/10.1039/c7se00423k>.
45. Dmello, R., Milshtein, J.D., Brushett, F.R., and Smith, K.C. (2016). Cost-driven materials selection criteria for redox flow battery electrolytes. *J. Power Sources* 330, 261–272. <https://doi.org/10.1016/j.jpowsour.2016.08.129>.
46. Darling, R.M., Gallagher, K.G., Kowalski, J.A., Ha, S., and Brushett, F.R. (2014). Pathways to low-cost electrochemical energy storage: a comparison of aqueous and nonaqueous flow batteries. *Energy Environ. Sci.* 7, 3459–3477. <https://doi.org/10.1039/C4EE02158D>.
47. Nightingale, E.R., Jr. (1959). Phenomenological theory of ion solvation. Effective radii of hydrated ions. *J. Phys. Chem.* 63, 1381–1387. <https://doi.org/10.1021/j150579a011>.
48. Xu, F., and Kameche, M. (2012). Transport of ions and solvent through a Nafion membrane modified with polypyrrole. *J. Membr. Sep. Technol.* 1, 108–116.
49. Zhang, Y., and Maginn, E.J. (2015). Direct correlation between ionic liquid transport properties and ion pair lifetimes: a molecular dynamics study. *J. Phys. Chem. Lett.* 6, 700–705. <https://doi.org/10.1021/acs.jpclett.5b00003>.
50. Sadakiyo, M., Yamada, T., and Kitagawa, H. (2014). Proton conductivity control by ion substitution in a highly proton-conductive metal-organic framework. *J. Am. Chem. Soc.* 136, 13166–13169. <https://doi.org/10.1021/ja507634v>.
51. Hellner, E., and Koch, E. (1982). The garnet-like cyanide framework of ammonium ferrocyanide hydrate with a channel system for ionic conductivity. *Acta Crystallogr. Sect. B* 38, 376–379. <https://doi.org/10.1107/S056774088200301X>.
52. Miao, W., Ding, Z., and Bard, A.J. (2002). Solution viscosity effects on the heterogeneous electron transfer kinetics of ferrocenemethanol in dimethyl Sulfoxide–water mixtures. *J. Phys. Chem. B* 106, 1392–1398. <https://doi.org/10.1021/jp013451u>.
53. Licht, S. (1985). pH measurement in concentrated alkaline solutions. *Anal. Chem.* 57, 514–519. <https://doi.org/10.1021/ac50001a045>.
54. Vanysek, P. (1993). Ionic conductivity and diffusion at infinite dilution. *CRC hand B. Chem. Phys.* 5–92.
55. Kwabi, D.G., Ji, Y., and Aziz, M.J. (2020). Electrolyte lifetime in aqueous organic redox flow batteries: a critical review. *Chem. Rev.* 120, 6467–6489.
56. Völz, H.G., Kischewitz, J., Woditsch, P., Westerhaus, A., Griebler, W.D., De Liedekerke, M., Buxbaum, G., Printzen, H., Mansmann, M., Råde, D., et al. (2000). Pigments, inorganic.

- Ullmann's Encycl. Ind. Chem. https://doi.org/10.1002/14356007.a20_243.
57. Himmelreich, U., and Kuchel, P.W. (1997). ^{13}C -NMR studies of transmembrane electron transfer to extracellular ferricyanide in human erythrocytes. *Eur. J. Biochem.* 246, 638–645. <https://doi.org/10.1111/j.1432-1033.1997.t01-1-00638.x>.
58. Balmaseda, J., Reguera, E., Fernández, J., Gordillo, A., and Yee-Madeira, H. (2003). Behavior of Prussian blue-based materials in presence of ammonia. *J. Phys. Chem. Solid.* 64, 685–693. [https://doi.org/10.1016/S0022-3697\(02\)00378-5](https://doi.org/10.1016/S0022-3697(02)00378-5).
59. Hansen, L.D., Litchman, W.M., and Daub, G.H. (1969). Turnbull's blue and Prussian blue: $\text{KFe(III)[Fe(II)(CN)}_6\text{]}$. *J. Chem. Educ.* 46, 46. <https://doi.org/10.1021/ed046p46>.
60. Ito, A., Suenaga, M., and Ono, K. (1968). Mössbauer study of soluble Prussian blue, insoluble Prussian blue, and Turnbull's blue. *J. Chem. Phys.* 48, 3597–3599. <https://doi.org/10.1063/1.1669656>.
61. Buser, H.J., Schwarzenbach, D., Petter, W., and Ludi, A. (1977). The crystal structure of Prussian blue: $\text{Fe}_4[\text{Fe}(\text{CN})_6]_3 \times \text{H}_2\text{O}$. *Inorg. Chem.* 16, 2704–2710. <https://doi.org/10.1021/ic50177a008>.
62. Sim, P.G., and Whalley, E. (1987). Mechanism of the reduction of potassium ferricyanide by shearing. *J. Phys. Chem.* 91, 1877–1878. <https://doi.org/10.1021/j100291a038>.
63. Neyhouse, B.J., Fenton, A.M., and Brushett, F.R. (2021). Too much of a good thing? Assessing performance tradeoffs of two-electron compounds for redox flow batteries. *J. Electrochem. Soc.* 168, 050501. <https://doi.org/10.1149/1945-7111/abeee3>.
64. Ben-Yaakov, D., Andelman, D., and Podgornik, R. (2011). Dielectric decrement as a source of ion-specific effects. *J. Chem. Phys.* 134, 074705. <https://doi.org/10.1063/1.3549915>.
65. Qing, L., Lei, J., Zhao, T., Qiu, G., Ma, M., Xu, Z., and Zhao, S. (2020). Effects of kinetic dielectric decrement on ion diffusion and capacitance in electrochemical systems. *Langmuir* 36, 4055–4064. <https://doi.org/10.1021/acs.langmuir.0c00353>.
66. Reber et al. The role of energy density for grid-scale batteries, <https://doi.org/10.26434/chemrxiv-2022-5ddhs>
67. Thurston, J.R., Marshak, M.P., and Reber, D. (2022). Monitoring ion exchange chromatography with affordable flame emission spectroscopy. *J. Chem. Educ.* <https://doi.org/10.1021/acs.jchemed.2c00455>.
68. Williams, H. (1912). Simple method for the production of pure ferrocyanides of the heavy metals. *Chem. world; a Mon. J. Chem. Chem. Eng.* 1, 43–44.
69. Dolomanov, O.V., Bourhis, L.J., Gildea, R.J., Howard, J.A.K., and Puschmann, H. (2009). OLEX2: a complete structure solution, refinement and analysis program. *J. Appl. Cryst.* 42, 339–341. <https://doi.org/10.1107/S0021889808042726>.
70. Bourhis, L.J., Dolomanov, O.V., Gildea, R.J., Howard, J.A.K., and Puschmann, H. (2015). The anatomy of a comprehensive constrained, restrained refinement program for the modern computing environment—Olex2 dissected. *Acta Crystallogr. A Found. Adv.* 71, 59–75. <https://doi.org/10.1107/S2053273314022207>.
71. Momma, K., and Izumi, F. (2011). VESTA 3 for three-dimensional visualization of crystal, volumetric and morphology data. *J. Appl. Cryst.* 44, 1272–1276. <https://doi.org/10.1107/S0021889811038970>.